The 9th European Congress on Computational Methods in Applied Sciences and Engineering
ECCOMAS Congress 2024
3–7 June 2024, Lisboa, Portugal

EXPERIMENTAL AND NUMERICAL INVESTIGATION OF THE MECHNAICAL BEHAVIOR OF SHORT FIBER REINFORECD ADHESIVES ECCOMAS CONGRESS 2024

M. HEMATIPOUR[1], A. DEAN[1,2], M. TARIQ[1], S. SCHEFFLER[1] AND R. ROLFES[1]

[1] Institute of Structural Analysis
Leibniz University Hannover
Appelstraße 9A, 30167 Hannover, Germany
e-mail: m.hematipour@isd.uni-hannover.de

[2] School of Civil Engineering, College of Engineering
Sudan University of Science and Technology
P. O. Box 72, Khartoum, Sudan
e-mail: a.dean@sustech.edu, www.sustech.edu

Key words: SFRP Composites, Structural Adhesives, Wind Turbine Blades, Experimental Test, Finite Element Method (FEM)

Summary. Structural adhesives are essential in various applications, particularly in the wind energy industry, where rotor blade components are joined using adhesives. Cracks in the bonding line of rotor blades indicate gaps in design and analysis knowledge. To address this, adhesives made of high-viscous epoxy polymers reinforced with short fibers have been developed to meet industry requirements. The performance of these Short Fiber Reinforced Polymeric (SFRP) adhesives depends significantly on fiber orientation. This study provides an experimental characterization of SFRP adhesives under tension, compression, and shear loads. Additionally, it introduces a finite-element framework for static analysis, with results thoroughly discussed and compared.

1 INTRODUCTION

Blade damages are the most frequent type of damage reported among different types of damage in the whole turbine [1]. Wind blades are major structural elements of wind turbines but they are prone to damage like any other composite component. Blade damage can cause sudden structural failure and the associated costs are very high. Therefore, it is important to identify the causation of damage to prevent defects during manufacturing phase, transport and in operation. It has been shown, that one of the frequently repeated types of blade damage is adhesive joint failure [2], see Fig. 1. Due to the location of the bonded joints and their importance for the integrity of the entire blade, the reliability of the bonded joints is of particular importance for the safe and economical operation of wind turbines. Structural adhesives, crucial in diverse applications, face major challenges particularly in wind energy industries. To take into account the complex loading conditions during the lifetime of a rotor blade and the manufacturing circumstances, adhesives have been developed to fulfill the specifications of the wind

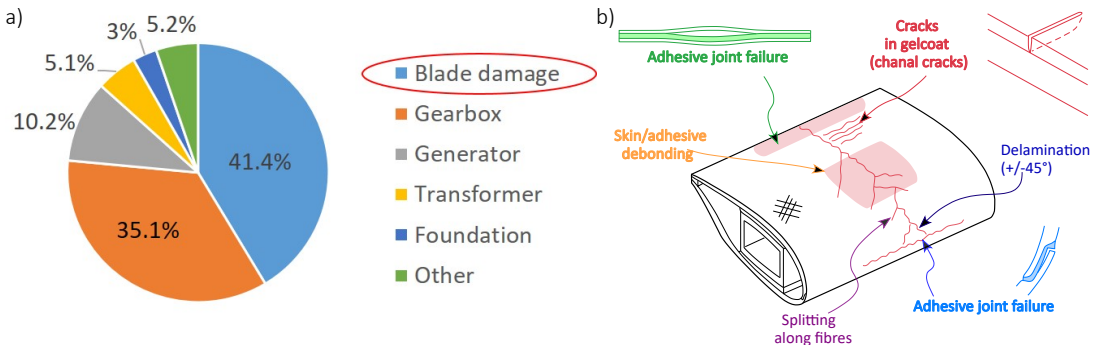

Figure 1: a) Most frequently reported damage in wind turbine [1] and b) summary of type of damage in the blades of wind turbines [2].

energy industry. These adhesives are typically composites made of high-viscous epoxy polymers reinforced with short glass [3]. Consequently, the mechanical performance of these adhesives strongly depends on the orientation of fibers. Mortazavian and Fatemi [4] studied the effects of fiber orientation and anisotropy on tensile properties of two short glass fiber reinforced plastics and observed that tensile strength and elastic modulus are significantly reduced from in-flow direction to perpendicular-to-flow direction at all temperatures and strain rates. De Monte et al. [5] studied the effect of mold flow direction on tensile behavior of short glass fiber polyamide-6.6 using 1, 2, and 3 mm thickness specimens with their axes at 0°, 10°, 20°, 30°, 45°, 60°, and 90° directions with respect to the mold flow direction. Tensile strength and elastic modulus decreased as the angle of specimen axis increased. Variation of elastic modulus with specimen axis was less pronounced for thicker specimens. Zarouchas et al [6] studied the mechanical behavior of thick structural adhesives under different loading conditions without considering the anisotropic response of the material. They have observed non-linear behaviour under tension, compression and torsion loading. In the related literature, numerous studies have focused on the theoretical formulation and numerical analysis of anisotropic plastic models[12, 13, 14]. Dean et al. [8] presented an invariant-based transversely isotropic thermo-plastic material model. For nonlinear material modeling, the plasticity algorithm utilized a non-associative flow rule, enabling the prediction of realistic plastic deformation.

Beside easy application as adhesives in complex geometries, like wind turbine blades, SFRP provide several further benefits. Adding short glass fiber to the resin will improve the mechanical properties such as flextural strength and cohesive parameter and due to deflecting the crack path and fiber bridging a longer fatigue life is expected. The fact, that cracks in the rotor blade structure, especially in the bonding line of the trailing edge, are causes of costly repairs and operational failures, indicates that there are still knowledge gaps in the analysis and design of such structures. The current contribution focuses on the experimental material characterization (under tension, compression and shear loading) and numerical investigation of the static behavior of SFRP adhesives. For the purpose of material characterization, firstly SFRP adhesive plates were manufactured. Specimens were then cut out from the fabricated plates using water-jet cutting in two different directions (0° and 90°). Finally, quasi-static tests were conducted for various loading conditions. Strain gauges and Digital Image Correlation (DIC) were used as measurement systems. Motivated from the progressive damage model developed in [7], and considering the elasto - plastic behavior of SFRP adhesives studied in [8], [9], a finite-element

framework for static analysis is introduced. In conclusion, the experimental and numerical results are presented, discussed, and compared.

2 EXPERIMENTAL INVESTIGATION

In this section, a comprehensive experimental characterization of SFRP adhesives is presented.

2.1 Adhesive system

For the experimental investigation, the EPIKOTE^{TM} Resin MGS^{TM} BPR 135G3 adhesive system was used in combination with EPIKURE^{TM} curing agent MGS^{TM} BPH 137G. The solvent-free system is epoxy-based and glass fiber-reinforced, which is very common in the wind energy industry. More detailed information on the resin/hardener mixing condition and related physical and mechanical data such as viscosity, glass transition development and mechanical behavior can be found on the technical data sheet of the adhesive [10]. The dimension of reinforcement fibers are not published.

2.2 Specimen production and experimental set-up

A planetary centrifugal mixer was used to obtain a homogeneous, pore-free mixture. The resin and hardener are placed in a mixing container, which spins on an incline while rotating normally. This whirling motion uniformly mixes the resin and hardener within minutes. The mixture was subsequently injected into a mold to produce plates with a thickness of 4 mm and cured at 75°C for four hours. Specimens were cut out from the fabricated plates using water-jet cutting at two different orientations relative to the injection direction: parallel and perpendicular. Specimen geometries and dimensions are reported in Fig. 2. The testing of the specimen has been conducted using a 100 kN servo-hydraulic testing machine. To measure the deformations of the specimens during testing, digital image correlation (DIC) device and strain gauges has been integrated into the test setup, see Fig. 3. To prepare for DIC measurements, the specimens were degreased, coated with white primer and subsequently sprackled with black paint to obtain a stochastic black and white pattern. The quasi-static tests were conducted with the speed of 1 mm/min.

2.3 Microcomputed tomography

To gain a comprehensive understanding of the internal arrangement of SFRP sheets, non-destructive CT examinations were conducted at the Institute for Wind Energy Systems, Leibniz University Hannover. This method enables full 3D image analysis using micro-computerized tomography (see Fig. 4). The μCT analysis reveals that the manufacturing process induces a preferred fiber orientation across the plate's thickness, with most fibers primarily aligned in the flow direction.

3 MATERIAL MODELING

This section focuses on the constitutive formulation of the anisotropic invariant-based model for SFRP composites. The anisotropic response of such materials is basically motivated by the production process and effect of flow direction on the fiber orientation, see Fig. 4.

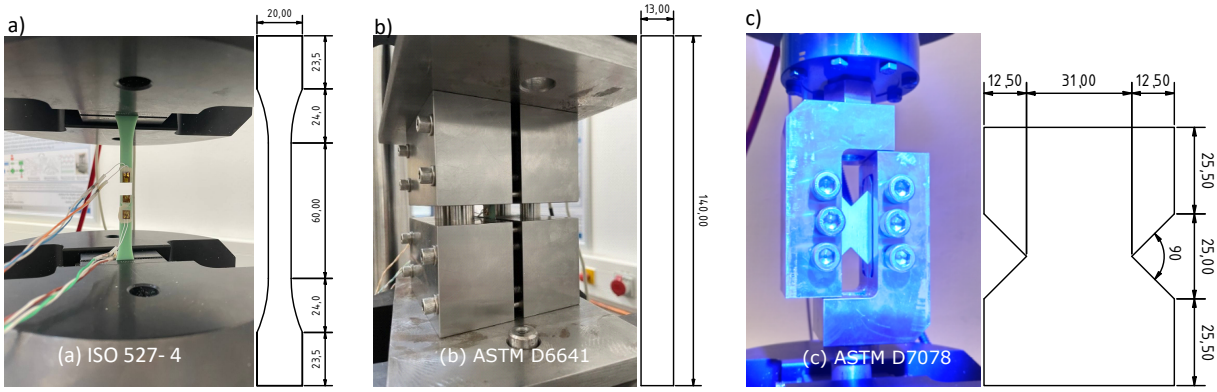

Figure 2: Test set-up, specimen geometry and dimensions in (mm): a) uniaxial tension DIN EN ISO 527-4, b) uniaxial compression ASTM D6641, and c) shear ASTM D7078.

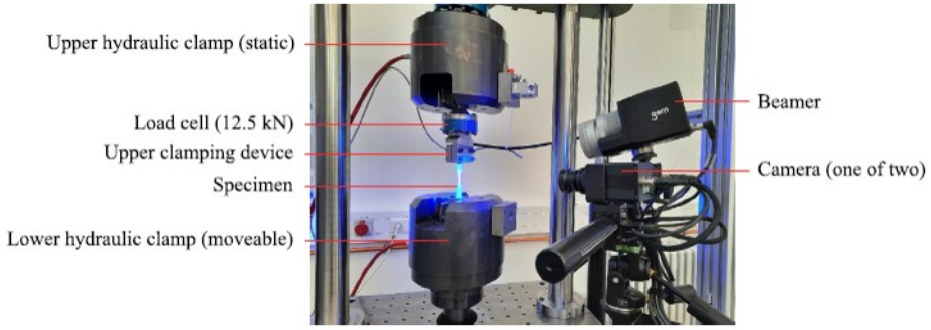

Figure 3: Photo of the set-up used for SFRP characterization tests.

At the macro-mechanical level, from a mathematical perspective, fibers orientations can be attained by means of a tensor-based representation, where the three dimensional fiber orientations is defined at material point level using the second-order tensor $\mathbf{A}$. This structural operator can be computed by applying the fiber distribution tensor to a group of n fibers in a limited range. Therefore, the structural tensor $\mathbf{A}$ can be defined as:

$$\mathbf{A} := \mathbf{a} \otimes \mathbf{a} \tag{1}$$

Here, $\mathbf{a}$ denotes the vector representing the preferential fiber orientation, which is the direction with the highest concentration of aligned fibers and coincides with the flow direction within the specimen. According to the representation in Eq. 1, the material's response remains unchanged under arbitrary rotations around $\mathbf{a}$, reflections in planes parallel to the fibers, and reflections in planes with a normal coinciding with $\mathbf{a}$.

3.1 Transversely isotropic free-energy definition

Defining the total strain tensor ($\boldsymbol{\varepsilon}$) as a symmetric part of the spatial displacement gradient ($\boldsymbol{\varepsilon} := \nabla^{s}\mathbf{u}$) and taking into account the infinitesimal deformation, the total strain tensor is

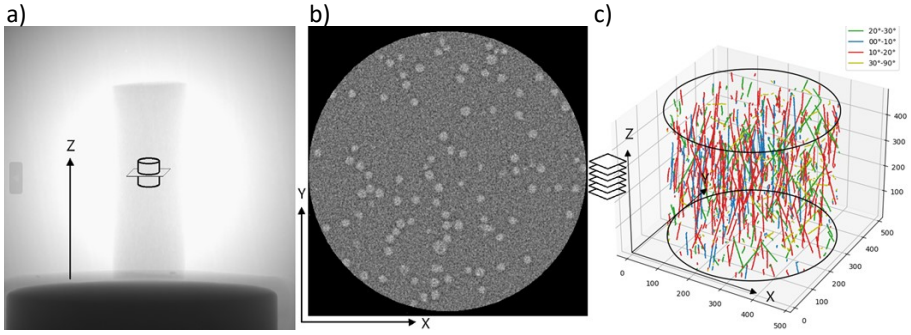

Figure 4: Micro-computed tomography of SFRP adhesive Specimen using injection molding procedure at 10x magnification: a) sample that was cut from the plate in the flow direction, b) section across the sample, with fibers shown as white dots, and c) distribution of fiber orientation in the sample.

additively decomposed into elastic ($\boldsymbol{\varepsilon}^{\mathrm{e}}$) and plastic ($\boldsymbol{\varepsilon}^{\mathrm{p}}$) counterparts as follows:

$$\boldsymbol{\varepsilon} = \boldsymbol{\varepsilon}^{\mathrm{e}} + \boldsymbol{\varepsilon}^{\mathrm{p}} \tag{2}$$

According to previous decomposition, the Helmholtz free-energy function Ψ can be defined as:

$$\Psi\left(\boldsymbol{\varepsilon}^{\mathrm{e}}, \alpha, \mathbf{A}\right) = \Psi^{\mathrm{e}}(\boldsymbol{\varepsilon}^{\mathrm{e}}, \mathbf{A}) + \Psi^{\mathrm{hard}}\left(\alpha\right) \tag{3}$$

where α stands for the set of variables that accounts for hardening of the system and Ψ^{hard} is the hardening part of free-energy function due to plastic deformation. A particular form of Eq. 3 for elasto-plastic material model reads:

$$\Psi(\boldsymbol{\varepsilon}^{\mathrm{e}}, \alpha, \mathbf{A}) = \frac{1}{2}\boldsymbol{\varepsilon}^{e} : \mathbb{C}^{\mathrm{e}} : \boldsymbol{\varepsilon}^{\mathrm{e}} + \Psi^{\mathrm{hard}}\left(\alpha\right) \tag{4}$$

where $\mathbb{C}^{e}$ identifies the elastic constitutive tensor, which is particularized to transversely isotropic response in the sequal (see Eq. 6). Considering the definition of Cauchy stress tensor σ as the first derivative of free-energy function with respect to the elastic strain tensor, the elastic constitutive operator $\mathbb{C}^{e}$ can be obtained as the second derivative of the free-energy with respect to elastic strain tensor:

$$\boldsymbol{\sigma} := \partial_{\boldsymbol{\varepsilon}^{e}}\Psi; \qquad \mathbb{C} := \partial_{\boldsymbol{\varepsilon}^{e}\boldsymbol{\varepsilon}^{e}}\Psi \tag{5}$$

For transversely isotropic materials, the elasticity operator can be expressed as:

$$\mathbb{C}^{e} := \partial_{\boldsymbol{\varepsilon}^{e}\boldsymbol{\varepsilon}^{e}}\Psi = \lambda\mathbf{1}\otimes\mathbf{1} + 2\mu_T\mathbb{I} + \left(\alpha\right)\left(\mathbf{1}\otimes\mathbf{A} + \mathbf{A}\otimes\mathbf{1}\right) + 2\left(\mu_L - \mu_T\right)\mathbb{I}_A + \beta\mathbf{A}\otimes\mathbf{A} \tag{6}$$

where $\mathbb{I}$ stands for the fourth-order identity tensor and $\mathbb{I}_{\mathrm{A}} = \mathrm{A}_{\mathrm{im}}\mathbb{I}_{\mathrm{jmkl}} + \mathrm{A}_{\mathrm{jm}}\mathbb{I}_{\mathrm{mikl}}$ where as λ, α, μ_T, and μ_L identify the elastic constants, whose definition and relationships with regards to the engineering constants are given in [11].

3.2 Yield function

The decomposition of the stress tensor $\boldsymbol{\sigma}$ into plasticity-inducing stresses $\boldsymbol{\sigma}^{\mathrm{pind}}$ and reaction stresses $\boldsymbol{\sigma}^{\mathrm{reac}}$ can be expressed as:

$$\boldsymbol{\sigma} := \boldsymbol{\sigma}^{\mathrm{reac}} + \boldsymbol{\sigma}^{\mathrm{pind}}; \quad \boldsymbol{\sigma}^{\mathrm{pind}} := \frac{1}{2}\left(\mathrm{tr}\left[\boldsymbol{\sigma}\right] - \mathbf{a}\boldsymbol{\sigma}\mathbf{a}\right)\mathbf{1} - \frac{1}{2}\left(\mathrm{tr}\left[\boldsymbol{\sigma}\right] - 3\mathbf{a}\boldsymbol{\sigma}\mathbf{a}\right)\mathbf{A} \tag{7}$$

where tr [] stands for the trace operator of a second-order tensor. The transversely isotropic yield surface which accounts for the plastic deformation along fiber direction can be expressed as follows:

$$f\left(\boldsymbol{\sigma}, \mathbf{A}, \bar{\varepsilon}^{\mathrm{p}}\right) = \zeta_1 I_1 + \zeta_2 I_2 + \zeta_3 I_3 + \zeta_4 I_3^2 + \zeta_5 I_4 + \zeta_6 I_4^2 - 1 \leq 0 \tag{8}$$

whereas $\bar{\varepsilon}^{\mathrm{p}}$ represents the equivalent plastic strain $\left(\bar{\varepsilon}^{\mathrm{p}} := \sqrt{\frac{2}{3}}\|\boldsymbol{\varepsilon}^{\mathrm{p}}\|\right)$ and $I_i (i = 1, 4)$ identifying the stress invariants, which are defined as:

$$I_1 = \frac{1}{2}\left(\mathrm{tr}\left[\boldsymbol{\sigma}^{\mathrm{pind}}\right]\right)^2 - \mathrm{tr}\left[\mathbf{A}\left(\boldsymbol{\sigma}^{\mathrm{pind}}\right)^2\right];\ I_2 = \mathrm{tr}\left[\mathbf{A}\left(\boldsymbol{\sigma}^{\mathrm{pind}}\right)^2\right]$$

$$I_3 = \mathrm{tr}\left[\boldsymbol{\sigma}\right] - \mathrm{tr}\left[\mathbf{A}\boldsymbol{\sigma}\right];\ I_4 = \frac{3}{2}\mathrm{tr}\left[\mathbf{A}\boldsymbol{\sigma}^{\mathrm{dev}}\right] \tag{9}$$

where $\boldsymbol{\sigma}^{\mathrm{dev}}$ denotes the deviatoric part of the stress tensor. The combination of six parameter $\zeta_i\left(\bar{\varepsilon}^{\mathrm{p}}\right), (i = 1, 6)$ and their corresponding invariants represents different mechanical loading state.

3.3 Plastic potential function

For a realistic representation of plastic deformation in SFRP composites at different loading states, a non-associative flow rule is implemented. Therefore, the evolution of the plastic strain is not governed by the gradient of the yield surface. This necessitates the definition of an invariant-based quadratic transversely isotropic plastic potential function g. Similar to the definition of the yield function, but without the linear terms associated with I_3 and I_4, the plastic flow function is assumed to take the form:

$$g\left(\boldsymbol{\sigma}, \mathbf{A}\right) = \xi_1 I_1 + \xi_2 I_2 + \xi_3 I_3^2 + \xi_4 I_4^2 - 1 \leq 0 \tag{10}$$

where $\xi_i (i = 1, 4)$ are the set of plastic potential parameters. The non-associative flow rule is used to realistically model plastic deformation behavior, particularly plastic contractility/dilatancy and plastic Poisson's coefficients. Thus, selecting appropriate plastic potential parameters is crucial.

3.4 Parameter identification

In order to determine the parameters that define the yield surface (Eq. 8) and the plastic potential function (Eq. 10), the elasto-plastic behavior of the material under consideration should be characterized. This section presents a summary of the equations used for parameter identification. For a more comprehensive description of the procedure followed in this study, the reader is referred to Vogler et al. [11] and Dean et al. [8, 9]. In the present case, the following experiments can be employed for the calibration of the implemented model: (i) in-plane shear test, (ii) transverse shear test, (iii) uniaxial longitudinal tension test, (iv) uniaxial longitudinal compression test, (v) uniaxial transverse tension test, and (vi) uniaxial transverse compression test. The corresponding yield stress states are denoted as $\sigma_{\mathrm{y}}^{\mathrm{is}}$, $\sigma_{\mathrm{y}}^{\mathrm{ts}}$, $\sigma_{\mathrm{y}}^{\mathrm{ft}}$, $\sigma_{\mathrm{y}}^{\mathrm{fc}}$, $\sigma_{\mathrm{y}}^{\mathrm{tt}}$, and

$\sigma_{\mathrm{y}}^{\mathrm{tc}}$, respectively. Following the described procedure in [11, 8, 9], the coefficients $\zeta_i, (i = 1, 6)$ are explicitly expressed as follows:

$$\zeta_1 = \frac{1}{(\sigma_{\mathrm{y}}^{\mathrm{ts}})^2}; \quad \zeta_2 = \frac{1}{(\sigma_{\mathrm{y}}^{\mathrm{is}})^2}; \quad \zeta_3 = -\frac{1}{2\sigma_{\mathrm{y}}^{\mathrm{fc}}} - \frac{1}{\sigma_{\mathrm{y}}^{\mathrm{tc}}} + \frac{1}{2\sigma_{\mathrm{y}}^{\mathrm{ft}}} + \frac{1}{\sigma_{\mathrm{y}}^{\mathrm{tt}}}$$

$$\zeta_4 = -\frac{1}{4\sigma_{\mathrm{y}}^{\mathrm{fc}}\sigma_{\mathrm{y}}^{\mathrm{ft}}} - \frac{1}{4(\sigma_{\mathrm{y}}^{\mathrm{ts}})^2} + \frac{1}{\sigma_{\mathrm{y}}^{\mathrm{tc}}\sigma_{\mathrm{y}}^{\mathrm{tt}}}; \quad \zeta_5 = -\frac{1}{\sigma_y^{fc}} + \frac{1}{\sigma_y^{ft}}; \quad \zeta_6 = \frac{1}{\sigma_{\mathrm{y}}^{\mathrm{fc}}\sigma_{\mathrm{y}}^{\mathrm{ft}}} \tag{11}$$

It must be noted that to comply the maximum dissipation principle, the convexity of yield surface must be insured. This imposes the following restrictions to the relations of $\zeta_i, (i = 1, 6)$ which should hold for any $\bar{\boldsymbol{\varepsilon}}^{\mathrm{p}}$:

$$\sigma_{\mathrm{y}}^{\mathrm{ft}}\sigma_{\mathrm{y}}^{\mathrm{fc}}\left[4\sigma_{\mathrm{y}}^{\mathrm{ts}2} - \sigma_{\mathrm{y}}^{\mathrm{tt}}\sigma_{\mathrm{y}}^{\mathrm{tc}}\right] \geq \sigma_{\mathrm{y}}^{\mathrm{tc}}\sigma_{\mathrm{y}}^{\mathrm{ts}2}\sigma_{\mathrm{y}}^{\mathrm{tt}} \tag{12}$$

As discussed earlier, the main motivation to adopt a non-associative plasticity rule is to model more realistic plastic deformation behavior. The four parameters of the plastic potential function can be determined accordingly. Similarly, these parameters control the shape and size of the surface of the plastic potential. However, the size of the plastic potential has no inherent physical meaning. Therefore, one of these parameters is a scaling parameter and can be set to any value. Here, ξ_1 is arbitrarily set to one and $\xi_i, (i = 2, 4)$ can be explicitly determined as follows:

$$\xi_1 = 1; \quad \xi_2 = \mu_{12}^{\mathrm{p}}; \quad \xi_3 = -\frac{-1 + \nu_{12}^{\mathrm{p}} + \nu_{23}^{\mathrm{p}}}{4(1 + \nu_{23}^{\mathrm{p}})}; \quad \xi_4 = \frac{\nu_{12}^{\mathrm{p}}}{1 + \nu_{23}^{\mathrm{p}}} \tag{13}$$

where $\nu_{12}^{\mathrm{p}} = \varepsilon_{11}^{\mathrm{p}}/\varepsilon_{22}^{\mathrm{p}}$ and $\nu_{23}^{\mathrm{p}} = \varepsilon_{22}^{\mathrm{p}}/\varepsilon_{33}^{\mathrm{p}}$ are representing the plastic Poisson's ratios and $\mu_{12}^{\mathrm{p}} = \varepsilon_{12}^{\mathrm{p}}/\varepsilon_{23}^{\mathrm{p}}$ represents the plastic distortion behavior.

4 RESULTS

This section focuses on presenting the results of the quasi-static tests and verifying and validating the implemented FE model.

4.1 Experimental results

In the first series of tests, two adhesives—one with short fiber reinforcement (SFRP) and one without (pure resin (PR))—were subjected to tensile and shear loading. The experimental results depicted in Fig. 5 demonstrate a notable improvement in mechanical properties by including short glass fiber reinforcement compared to pure resin.

4.1.1 Tension test

For the characterization of the SFRP adhesives, 0° and 90° (to the direction of molding) uniaxial quasi-static tension tests were carried out according to DIN EN ISO 527–4 [15]. For this purpose, the standard dog bone shaped specimen type 1B was used, see Fig. 2. The local strains were recorded using strain gauges and DIC measurement system. The experimental results are plotted in Fig. 6, where an anisotropic elasto-plastic material behavior of the SFRP is observed.

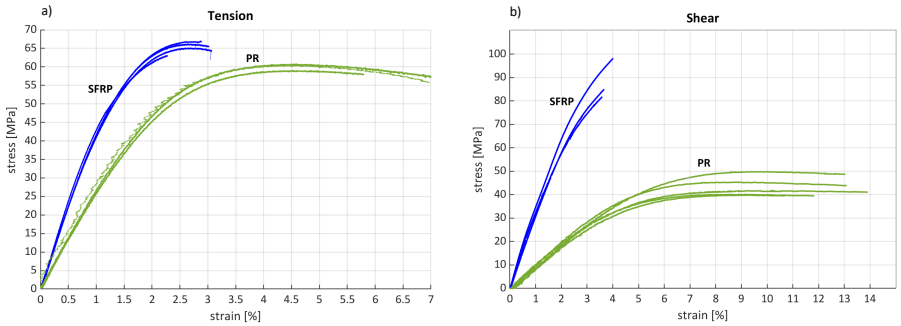

Figure 5: Comparison of mechanical properties of pure resin and short fiber reinforced adhesive in a) tension and b) shear.

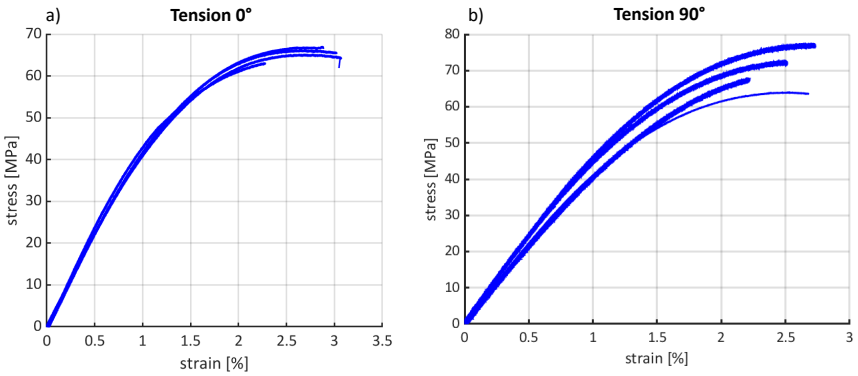

Figure 6: Result of tensile tests for SFRP adhesives: a) specimen in flow direction and b) perpendicular to flow direction.

4.1.2 Compression test

To investigate the behavior of SFRP adhesives under compressive loading, uniaxial quasi-static compression tests at 0° and 90° to the molding direction were conducted according to ASTM D6641 [16]. The specimens used demonstrated notable stability against early buckling during compression testing, see Fig. 2. Local strains were measured using strain gauges, and the experimental results are presented in Fig. 7. Similar to the tension test results, an anisotropic elasto-plastic material behavior of the SFRP is observed.

4.1.3 Shear test

To study the behavior of SFRP adhesives under in-plane shear stress state, 0° and 90° quasi-static V-Notched rail shear test were performed according to ASTM D 7078 [17]. The shear test fixture is introduced in Fig. 2 and the local strains on the shear zone were recorded using DIC. The experimental results are shown in Fig. 8. similarly, an anisoptropic elasto-plastic material behavior is observed.

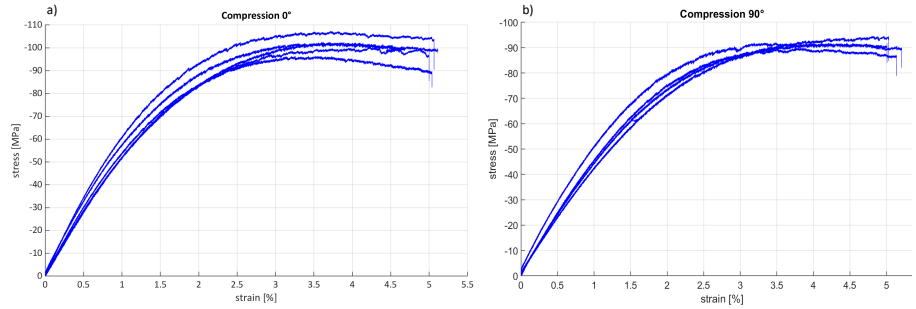

Figure 7: Result of compression tests for SFRP adhesives: a) specimen in flow direction and b) perpendicular to flow direction.

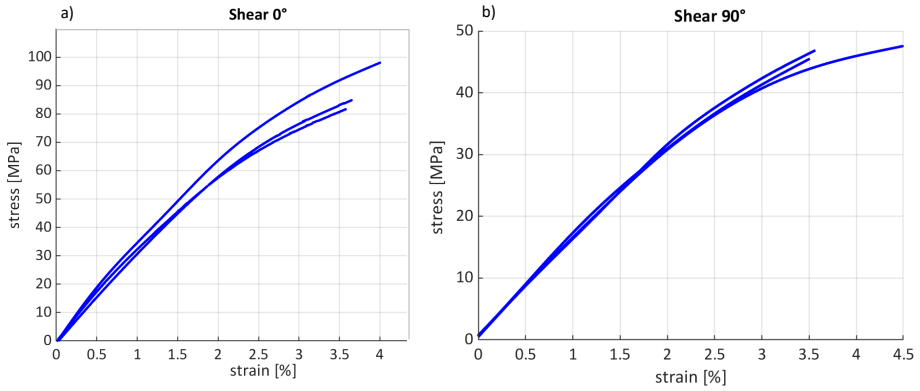

Figure 8: Result of shear tests for SFRP adhesives: a) specimen in flow direction and b) perpendicular to flow direction.

4.2 Numerical results

The previously described constitutive modeling is implemented into the commercial FE code ABAQUS using the user-defined subroutine UMAT. The goal of this section is to evaluate and verify the performance of the proposed formulation via the FE simulation.

4.2.1 FE simulation: model verification

Herein, the validity and potential of the proposed formulation are evaluated through a single element FE model. The side length of the SFRP 3D brick element is set to 1 mm. Five load cases are considered, with the flow direction as the reference: (i) longitudinal uniaxial tension, (ii) transverse uniaxial tension, (iii) longitudinal uniaxial compression, (iv) transverse uniaxial compression, and (v) in-plane shear. The numerical results are depicted in Fig.9. In this diagram, it is evident that during the initial development phase, before the material strength is reached, the non-linearities are modeled under the assumption of elasto-plastic behavior, prior to failure.

The model's ability to predict the anisotropic asymmetric behavior observed in SFRP is clearly demonstrated. Moreover, there is a strong agreement between the experimental data and the numerical predictions. These results validate the proposed numerical implementation,

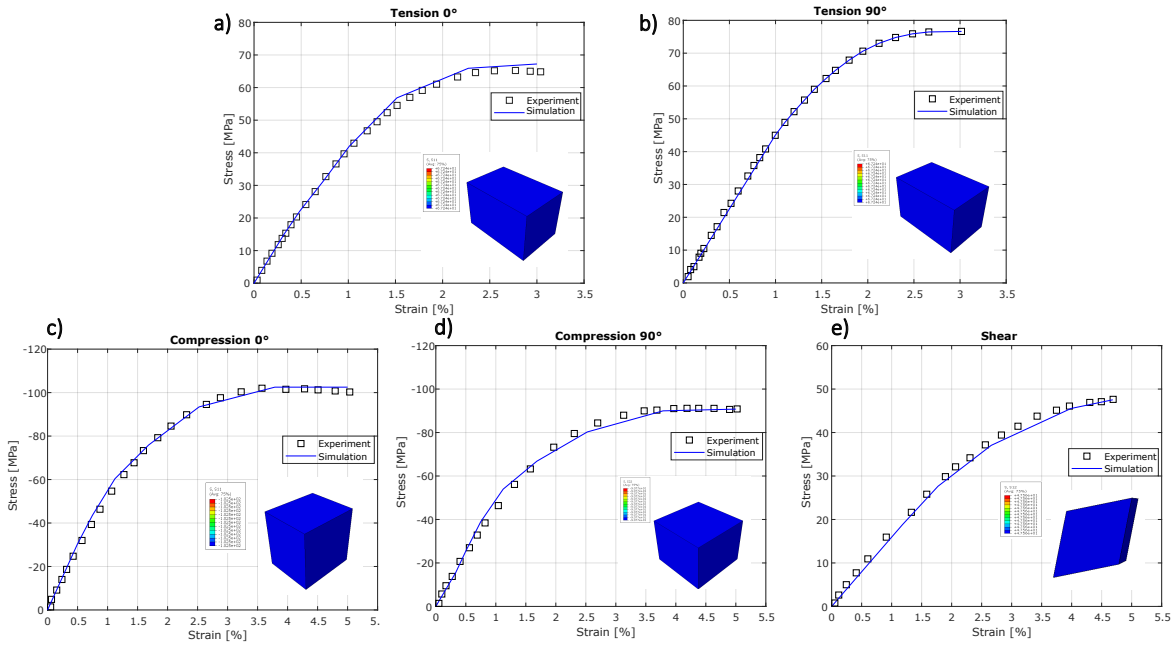

Figure 9: Numerical simulations vs experimental results: a) longitudinal uniaxial tension, b) transverse uniaxial tension, c) longitudinal uniaxial compression, d) transverse uniaxial compression, and e) in-plane shear.

accurately capturing the nonlinear material behavior at different stages of evolution and across various material directions.

4.2.2 FE simulation: model validation

In order to evaluate the reliability of the current FE model, a uniaxial quasi-static tensile test at 0° along the fiber direction is investigated on a 4 mm thick dog bone specimen made of SFRP. The definition of the specimen in terms of geometry, FE discretization and boundary conditions is shown in Fig. 10. A total of 12500 linear 3D brick elements with 8 nodes and reduced integration are used, with 4 elements distributed across the thickness. The boundary conditions imposed onto the FE model replicate those imposed in the experimental investigations: (i) restrained displacements and rotations at the clamped edge, and (ii) constrained displacements and rotations at the loaded edge except the prescribed displacement along the loading direction x. Fig.10 illustrates the experimental-numerical correlation of the load-displacement behavior up to the onset of failure. This graph demonstrates a high degree of agreement between the experimental data and numerical predictions, with only minor deviations observed in the elasto-plastic response prior to the initiation of damage.

5 CONCLUSIONS

This paper has two main objectives: experimentally characterizing short glass fiber reinforced adhesives and numerically modeling them. First, non-destructive and destructive tests examined the adhesives' anisotropy and mechanical behavior under different loading conditions,

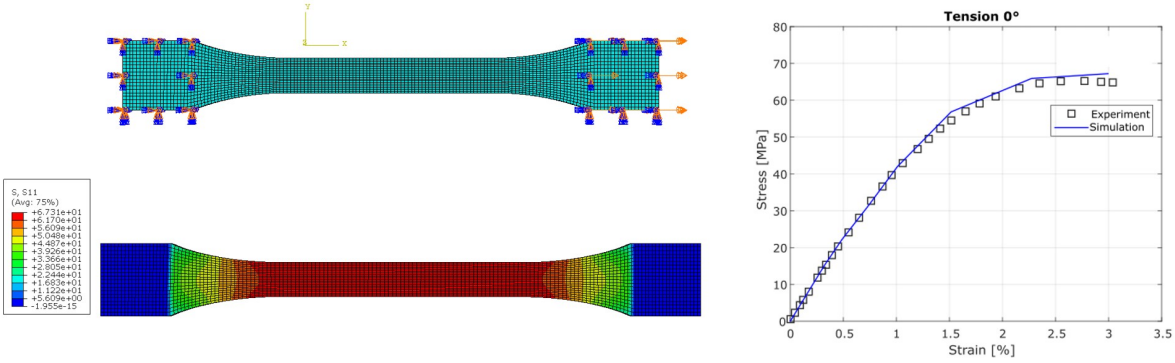

Figure 10: Experimental–numerical correlation of longitudinal tension tests.

with results thoroughly discussed. Second, the numerical modeling used an invariant-based anisotropic constitutive model, briefly explaining parameter identification. The model was calibrated through finite element simulations and used to simulate tensile tests on dog-bone-shaped specimens, showing strong experimental-numerical correlation. Future research will investigate the adhesives' fatigue behavior and develop the progressive fatigue damage model [18, 19] to include the non-linear behavior of SFRP adhesives.

REFERENCES

[1] M. Shohag, E. Hammel, DO. Olawale, OI. Okoli, Damage mitigation techniques in wind turbine blades: A review, Wind Engineering. 2017; 41(3):185-210, doi:10.1177/0309524X17706862

[2] B. Sørensen, P. Brøndsted. Reliability of Wind Turbine Blades: An Overview of Materials Testing, Wind Power Shanghai 2007

[3] M. Wentingmann, N. Manousides, A. Antoniou, C. Balzani, Design and manufacturing optimization of epoxy-based adhesive specimens for multiaxial tests; Materials, Design 212 (2021) 110213, https://doi.org/10.1016/j.matdes.2021.110213

[4] S.V. Mortazavian, Fatemi. Effects of fiber orientation and anisotropy on tensile strength and elastic modulus of short fiber reinforced polymer composites, Composites: Part B. 2015;72:116–29, http://dx.doi.org/10.1016/j.compositesb.2014.11.041

[5] M. De Monte, E. Moosbrugger, M. Quaresimin, Influence of temperature and thickness on the off-axis behaviour of short glass fibre reinforced polyamide 6.6-Quasi-static loading, Composites: Part A 41 (2010) 859–871, doi:10.1016/j.compositesa.2010.02.018

[6] D. Zarouchas, R. Nijssen, Mechanical behaviour of thick structural adhesives in wind turbine blades under multi axial loading, Journal of Adhesion Science and Technology,2016, 30:13, 1413-1429, DOI: 10.1080/01694243.2016.1146392

[7] C. Gerendt, A. Dean, T. Mahrholz, R. Rolfes, On the progressive failure simulation and experimental validation of fiber metal laminate bolted joints, Composite Structures 229 (2019) 111368, https://doi.org/10.1016/j.compstruct.2019.111368

[8] A. Dean, J. Reinoso, S. Sahraee, R. Rolfes, An invariant-based anisotropic material model for short fiber-reinforced thermoplastics: Coupled thermo-plastic formulation, Composites: Part A 90 (2016) 186–199, http://dx.doi.org/10.1016/j.compositesa.2016.06.015

[9] A. Dean, N. Grbic, R. Rolfes, B. Behrens, Macro-mechanical modeling and experimental validation of anisotropic, pressure- and temperature-dependent behavior of short fiber composites, Composite Structures 211 (2019) 630–643, https://doi.org/10.1016/j.compstruct.2018.12.045

[10] $Hexion^{TM}$, Technical data sheet- $EPIKOTE^{TM}$ Resin MGS^{TM} BPR 135G3-Series and $Epikure^{TM}$ curing agent MGS^{TM}BPH 137G

[11] M. Vogler, Anisotropic material models for fiber reinforced polymers, Ph. D. thesis. Hannover (Germany): Institute of Structural Analysis, Leibniz Universität Hannover, 2014

[12] A. Amiri-Rad, L.V. Pastukhov, L.E. Govaert, et al., An anisotropic viscoelastic-viscoplastic model for short-fiber composites, Mechanics of Materials 137 (2019) 103141. https://doi.org/10.1016/j.mechmat.2019.103141

[13] T.B. Van Erp, C.T. Reynolds, T. Peijs, et al., Prediction of yield and long-term failure of oriented polypropylene: kinetics and anisotropy. Journal of Polymer Science: Part B: Polymer Physics, Vol. 47, 2026–2035 (2009), DOI: 10.1002/polb.21801

[14] D.J.A. Senden, G.W.M. Peters, L.E. Govaert, J.A.W. Van Dommelen, Anisotropic yielding of injection molded polyethylene: experiments and modeling, Polymer 54 (2013) 5899-5908, http://dx.doi.org/10.1016/j.polymer.2013.08.047

[15] International Organization for Standardization. Plastics – determination of tensile properties. ISO 527-1, REV. 1997

[16] American Society for Testing and Materials, Standard Test Method for Compressive Properties of Polymer Matrix Composite Materials Using a Combined Loading Compression (CLC) Test Fixture, REV.2017

[17] American Society for Testing and Materials,Standard Test Method for Shear Properties of Composite Materials by V-Notched Rail Shear Method, REV. 2005

[18] C. Gerendt, A. Dean, T. Mahrholz, N. Englisch, S. Krause, R. Rolfes, On the progressive fatigue failure of mechanical composite joints: Numerical simulation and experimental validation, Composite Structures 248 (2020) 112488, doi.org/10.1016/j.compstruct.2020.112488

[19] C. Gerendt, M. Hematipour, N. Englisch, S. Scheffler, R. Rolfes, A finite element-based continuum damage model for mechanical joints in fiber metal laminates under static and fatigue loading, Composite Structures 312 (2023) 116797, doi.org/10.1016/j.compstruct.2023.116797